Computational Materials Science 144 (2018) 139–146

Contents lists available at ScienceDirect

Computational Materials Science

journal homepage: www.elsevier.com/locate/commatsci

Transparency enhancement for $SrVO_3$ by $SrTiO_3$ mixing: A first-principles study

Z.T.Y. Liu [a], N.J. Podraza [a], S.V. Khare [a,*], P. Sarin [b]

[a] Department of Physics and Astronomy, University of Toledo, Toledo, OH 43606, USA
[b] School of Materials Science and Engineering, Oklahoma State University, Tulsa, OK 74106, USA

ARTICLE INFO

Article history:
Received 4 July 2017
Received in revised form 23 October 2017
Accepted 12 December 2017

Keywords:
Transparent conducting oxides
Density functional theory
Phase diagrams
Cluster expansion
Dielectric function
Absorption spectra

ABSTRACT

$SrVO_3$ was recently found to be a strong candidate for transparent conducting oxide (TCO) applications. However, there is still a noticeable range of the blue spectrum that is not part of the transparency window. In response to that, we have studied the mixing of $SrVO_3$ and $SrTiO_3$ with density functional theory, cluster expansion, Monte Carlo simulations and special quasi-random structures (SQS). We confirmed with thermodynamics modeling the feasibility of obtaining solid solutions $SrTi_{1-x}V_xO_3$ across the full composition range ($0 \leq x \leq 1$). A simple miscibility gap closes at consolute temperature $T_C = 500$ K. Phase boundaries show slight asymmetry skewing toward the larger cation $SrTiO_3$-side. Electronic density of states and optical properties, including complex dielectric function spectra and band structures of the random solid solutions were studied with SQS. Substitution of V with Ti reduces the electrical conductivity of $SrTi_{1-x}V_xO_3$, which goes through a composition-driven metal to insulator transition close to $x = 0.67$, but suppresses the optical absorption beyond 3.25 eV. It is likely that doping or vacancy creation would enhance the electrical conductivity and extend the conducting compositions, leaving room for property tuning to obtain optimal TCO materials.

1. Introduction

The development of transparent conductors for solar cell, light emitting, and display technologies requires combining two seemingly contradicting material properties: high optical transparency and high electrical conductivity. Among them, transparent conducting oxides (TCO) have been widely researched [1–5]. Usually, a material that excels at one aspect does not do well at the other. Traditional approaches to fabricating 10 s–100 s nm thick transparent conducting layers include heavily doping wide-gap semiconductors, adding free carriers to a transparent base material, such as degenerately doped indium tin oxide (ITO) [3]. The added carriers turn the semiconductor base material into a conductor, but there are limits as to the concentration of dopants, self-compensation [2] as well as reduced total scattering time by impurities [1]. Recently a new approach was proposed [1], taking advantage of strong electron-electron interactions in highly correlated transition metal oxides [6–13], such as $SrVO_3$ and $CaVO_3$ [1]. These TCO materials have their Fermi energy levels in the conduction band edge and are therefore already conducting. The energies of interband optical transitions are primarily above 2.8 eV, extending into and above the blue region of the visible spectrum near 3.25 eV. The strong electronic correlation in these materials flattens the conduction band and increases the carrier effective mass, therefore reducing the energy scale of intraband transitions, limiting absorption on the red end of the visible spectrum near 1.75 eV. The outcome is a window containing the visible spectrum with low absorption present. Conductivity is in turn negatively influenced relative to metals, but is better than that of degenerately doped wide band gap semiconductors like ITO with a magnitude of 10^4 S cm^{-1}. The "correlated metal" approach potentially provides a better trade-off between optical transparency and electrical conductivity as well as alleviating the dependency on highly priced indium.

However, the optical absorption of $SrVO_3$ on the higher-energy part of the visible spectrum, starting from 2.8 eV, is not optimal. There is still a noticeable range of the blue spectrum that is not part of the transparency window. Improved transparent conductor performance would be obtained if absorption due to interband transitions can be blue-shifted to higher photon energies or suppressed in magnitude. One possible approach is mixing this material with a wide-gap semiconductor of similar structure and volume, such as $SrTiO_3$. Both compounds adopt the ideal perovskite structure. Ti is one group earlier than V, with an ionic radius [14] of Ti^{4+}, 0.61 Å, very close to that of V^{4+}, 0.58 Å. As a

* Corresponding author.
E-mail address: sanjay.khare@utoledo.edu (S.V. Khare).

https://doi.org/10.1016/j.commatsci.2017.12.020
0927-0256/

Table 1
Lattice parameters a, volumes per formula unit (V/f.u.), and bulk moduli (B) from EOS's of $SrTiO_3$ and $SrVO_3$.

	a (Å)	V/f.u. (Å^3)	B (GPa)
$SrTiO_3$	3.94	61.3	168
expt.[a]	3.905	59.55	184
calc.[c]	3.946	61.42	172.8
$SrVO_3$	3.89	58.8	175
expt.[b]	3.841	56.67	
calc.[c]	3.866	57.79	181.5

[a] Ref. [94].
[b] Ref. [95].
[c] FP-LAPW-GGA [112].

result, their unit-cell volumes are close too, calculated to be 61.3 Å^3 and 58.8 Å^3 (Table 1). $SrTiO_3$ has a rather large band gap of 3.25 eV [15] with interband transitions above. Previously experimental results showed that synthesis of solid solutions of the two in the full composition range is feasible [16–18]. Tsuiki et al. first demonstrated it with heat treatment of powders of $SrCO_3$, TiO_2 and V_2O_5 at 900–1100 °C under a flowing H_2 atmosphere and hydrostatic pressing at 100 MPa [16]. They measured the temperature-dependent conductivity, metal-nonmetal transition composition and the depth of the donor level of V^{4+} in $SrTiO_3$ [17]. Hong et al. used a higher temperature, 1550 °C and obtained similar results. Gu et al. grew epitaxial thin films using a pulsed electron-beam deposition (PED) technique at 800 °C [18]. Although conductivity was studied, optical properties were not. We intend to computationally study if the solid solutions could tune the absorption behaviors.

In this work, we study the thermodynamics of mixing $SrVO_3$ and $SrTiO_3$ with cluster expansion (CE) and Monte Carlo (MC) simulations to examine and validate the viability of obtaining $SrTi_{1-x}V_xO_3$ solid solutions across the full composition range ($0 \le x \le 1$). The cluster expansion formalism [19–24] is a first-principles approach to construct complete thermodynamic models to predict phase relations without resorting to experimental input. It fits the formation energies of a small number of structures (~50–100) calculated with density functional theory (DFT) to produce a set of effective cluster interactions (ECIs) for pairs, triplets, quadruplets, etc. This approach has been used to study a diverse set of material systems including alloys [25–32], semiconductors [33–36], ionic compounds [37–41], and minerals [42–46] yielding results that agree well with experiments. We then study electronic and optical properties, including complex dielectric function spectra, band structures, and electronic density of states (DOS) of the end members and random solid solutions with special quasi-random structures (SQS) [47,48]. SQS has also been used for a wide range of material systems and structures, both metal alloys [27,48–54] and ceramics [33,55–71], including peroxides [72,73]. We aim to explore the effects of mixing $SrVO_3$ with $SrTiO_3$ and whether it can suppress absorption near and beyond 2.8 eV, leaving the entire visible spectrum within the transparency window, and how much it adversely affects electrical conductivity.

2. Computational methods

We performed *ab initio* DFT computations with the Vienna Ab-initio Simulation Package (VASP) [74–77]. The projector-augmented wave method (PAW) [78,79] and Purdew–Burke–Ernzerhoff (PBE) generalized gradient approximation (GGA) [80,81] were used. Potentials of Sr_sv, Ti_sv, V_sv and O were selected, where "_sv" denotes that the semi-core s and p electrons are also included. Because transition metal oxides are correlated materials, the GGA + U correction scheme was used for the d orbitals of V with U = 4 eV, a choice made by comparing the complex dielectric function spectra under different parameter sets (potentials, spin-polarization and U values) in Sec. A of the Supplemental Materials. We adjusted our choice of the U value to match the high-energy part of the visible spectra starting from 2.8 eV, which was well-modeled with FM/U = 0 in Ref. [1]. Spin-polarization was not considered due to the abrupt change of the V^{4+} magnetic moments, spin channel separation and non-matching visible spectra with the GGA + U scheme. The Heyd-Scuseria-Ernzerhof hybrid functional (HSE06) did not improve the modeling of the visible spectra either, with or without spin-polarization. The GGA + U scheme for Ti however, was not used for the energy landscape calculations as per previous calibration work [82,83], but was used for electronic and optical calculations in Sections 3.4 and 3.5. A more detailed justification on our choice of a large U value is given in Section 3.3. The plane wave energy cutoff was chosen to be 400 eV for fixed cell volume & shape calculations and 520 eV for variable cell volume & shape relaxations. The k-point meshes were created with k-points per reciprocal atom (KPPRA) [84] of 1000 (Γ-centered $2 \times 2 \times 2$) for relaxations and 4000 (Γ-centered $4 \times 4 \times 4$) for electronic DOS and complex dielectric functions. Gaussian smearing was used with a σ value as small as 0.1 eV. For structural optimization, the atomic positions were allowed to relax until forces on any atom were below 0.02 eV/Å.

We first obtained equations of state (EOS's) for $SrTiO_3$ and $SrVO_3$. In each case, we picked 5 vol points, fitted the total energies to the Birch-Murnaghan EOS [85], and derived the equilibrium volumes (V_0) and bulk moduli (B) [86–89].

Next we used the Alloy Theoretic Automated Toolkit (ATAT) [90–93] to calculate the phase diagram of $SrTi_{1-x}V_xO_3$. Included in ATAT, the MIT Ab-initio Phase Stability (maps) [90,91] code was used to generate the energy landscape and CE. The Easy Monte Carlo Code (emc2 and phb) [92,93] was used to perform MC simulations to obtain the phase diagrams. Ground-state analysis was performed by using a well-converged CE to calculate formation energies (ΔE_f) for all 188,728 symmetrically inequivalent structures with 16 or fewer variable cation sites. In addition, we evaluated ΔE_f of the structures corresponding to random solid solution configurations at different compositions and fitted them to a smooth curve.

To obtain the phase diagram from CE, a box of $16 \times 16 \times 16$ 5-atom unit cells (4096 exchangeable sites) was chosen in the semi-grand canonical ensemble simulation. In such an ensemble chemical potential (μ) and temperature (T) can be given as external conditions. Chemical potential is defined as $\mu_i = (\partial G/\partial n_i)_{T,n_{j\neq i}}$, where G is the Gibbs free energy, n_i is the number of atoms of species i in the simulation cell. In a binary system $A_{1-x}B_x$, $\mu = \mu_A - \mu_B$ is used as the input. For each μ and T point, sufficient MC passes were used to make sure the composition (x) reached a precision of 0.01.

Electronic and optical properties were studied through energy/frequency-dependent complex dielectric function spectra from 0.4 to 6 eV. For random solid solution configurations of the mixed system $SrTi_{1-x}V_xO_3$, we employed SQS's, also used in other peroxides [72,73], at different compositions x = 1/9, 2/9, . . ., 8/9. Each SQS is a supercell of $3 \times 3 \times 3$ 5-atom unit cells (27 exchangeable sites). Extensive testing suggested they are adequate, and necessarily large to model randomness. These structures were obtained from the Monte Carlo generator of Special Quasirandom Structures (mcsqs) [48] code in ATAT. The maximum pair cluster diameter was set to 7 Å and triplet to 6 Å. For each composition, four instances of stochastic searches were performed and sufficient time was allowed to obtain the same structure closest to a random configuration. These prototype structures are provided in the Supplemental Materials. For each composition, we obtained the EOS using the method described above for the end members, relaxing only the ionic positions at each volume point, and did another ionic

relaxation at the equilibrium volume point determined from the EOS. The resultant equilibrium structures were used to calculate electronic DOS and complex dielectric function spectra.

3. Results and discussion

3.1. Cell parameters of the end members

Table 1 shows the lattice parameters of $SrTiO_3$ and $SrVO_3$. Volumes are given for the 5-atom formula unit. Lattice parameters (a) and volumes per formula unit (V) compare well with experimental results [94,95] with a small and consistent overestimation (<1%), while values of B obtained from the EOS fitting show an underestimation (<10%) [94]. These deviations are due to the use of GGA in our DFT calculations and is a well-known consequence of this approximation [69–71,86,87,96–111]. They are closer to other reported values calculated with GGA [112]. Note the slightly larger deviation of *a* and B of $SrVO_3$ than those of $SrTiO_3$, which arises from employing the GGA + U scheme to account for the correlation effect in $SrVO_3$.

3.2. Cluster expansions and phase diagrams

Fig. 1 shows the formation energy landscape of $SrTi_{1-x}V_xO_3$. All 36 non-end-member structures have positive DFT-calculated ΔE_f, below 60 meV/f.u. CE was performed and 4 pairs + 6 triplets were chosen to be the optimized cluster set with a cross validation score of 5 meV. Detailed information of the cluster set is provided in the Supplemental Materials. The top of the curve corresponding to random structures is ~25 meV, on the level of RT (0.02 eV at 298 K). Therefore, mixing should be feasible. A more accurate estimate can be derived with phase diagram calculations below. As a comparison, mixing $BaTiO_3$ with $CaTiO_3$ results in the top of the curve >140 meV, while mixing $BaTiO_3$ with $SrTiO_3$ results in 6 meV [113]. The $\Delta E_f(x)$ curve of random solid solution configurations shows asymmetry, skewing toward the larger cation $SrTiO_3$-side. Usually, the curve would lean to the smaller cation side, because it is more difficult to put a large ion into the smaller ion's lattice than vice versa, but we see the opposite here, likely due to the correlation effect of V^{4+} in oxides.

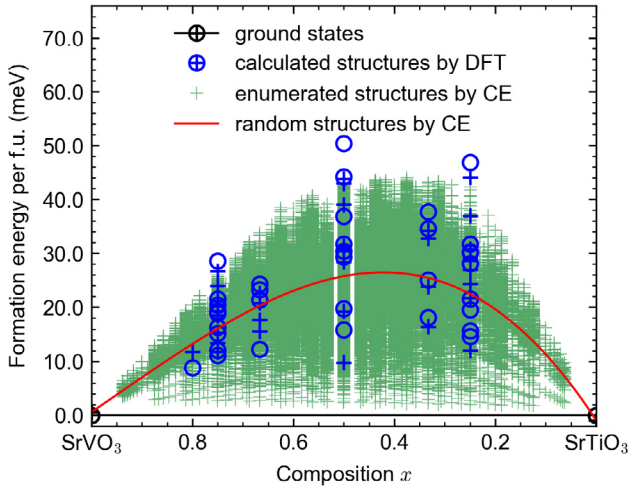

Fig. 1. The formation energy landscape of $SrTi_{1-x}V_xO_3$. Energy values are per formula unit, i.e. per exchangeable site. Black markers and the convex hull line indicate ground states, blue markers indicate the structures calculated with DFT and used to obtain the CE, and green crosses indicate a 16-exchangeable-site ground-state analysis. Among the markers, hollow circles indicate DFT values, and crosses indicate CE-fitted values. The red curve indicates CE-fitted values of the random solid solution configurations. (For interpretation of the references to colour in this figure legend, the reader is referred to the web version of this article.)

The calculated phase diagram with a simple miscibility gap is shown in Fig. 2. Depending on the composition x of interest, full solid solutions form at different temperatures. The top of the phase boundary, close to x = 0.4, is around 500 K. The nature of the miscibility gap in this perovskite solid solution is primarily lattice mismatch, as is also the case for other simple solid solutions with large lattice mismatches, e.g. carbonites [46] and transition metal nitrides [41]. In addition, a previous Born-Haber-like breakdown of the mixing process in CaO-MgO and $CaCO_3$-$MgCO_3$ indicates that chemical identity exchange contributes to small and slightly negative energy (in favor of mixing). Asymmetry in the $\Delta E_f(x)$ curve of the random solid solution configurations is also seen in the phase diagram, which is skewed toward the $SrTiO_3$-side. Although T_C is above the room temperature, there are ways to obtain the random solid solutions beyond 500 K and prevent the bulk solid solutions from phase separation as temperature decreases, because at these relatively low temperatures phase separation kinetics are low. As stated in Section 1, previous experimental endeavors were successful in synthesizing solid solutions of the entire composition range [16–18] by initially applying a much higher temperature (>1000 °C), one that lies in the fully miscible region in the phase diagram. This feature is useful for tuning various properties of the solid solutions.

3.3. GGA+U treatment for $SrTiO_3$

To correctly reproduce optical properties of $SrTiO_3$, there is also the consideration of GGA + U for Ti. Although Ti^{4+} has no d electrons, regular GGA does not result in the correct band gap. In Fig. 3 we show the energy-dependent complex dielectric function ($\varepsilon = \varepsilon_1 + i\varepsilon_2$) spectra for $SrTiO_3$ and in Fig. 4 band structures calculated with different parameter sets. Three variations are given: U = 0 or 10 eV with PBE potentials or using HSE06. PBE/U = 0 greatly underestimates the band gap, calculated to be 1.80 eV, while HSE06 produces a more accurate value, 3.26 eV (expt. 3.25 eV [15]). Comparing Fig. 4(a) and (c), the entire conduction bands, including the lower-lying Ti-t_{2g} and higher-lying Ti-e_g bands are up-shifted, leading to a blue-shifted ε_2 rise in Fig. 3. With PBE, we adjust U to match the HSE06 value, taking U = 10 eV, which leads to a band gap of 3.25 eV. Comparing Fig. 4(a) and (b), only Ti-t_{2g} bands are up-shifted while keeping the lower-lying O-p and higher-lying Ti-e_g bands intact. This results in the valley filling

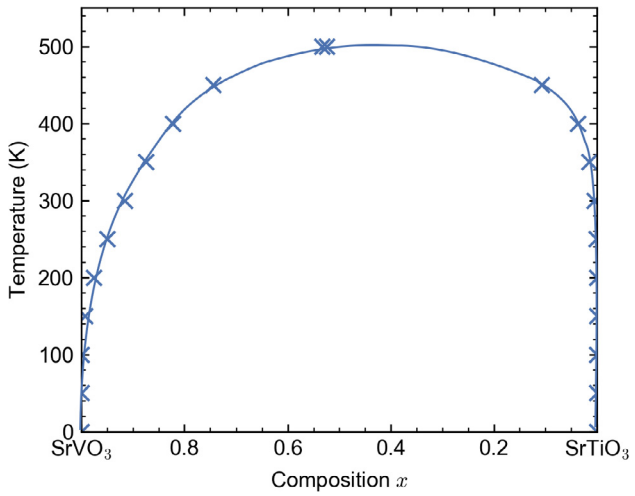

Fig. 2. Calculated phase diagrams of $SrTi_{1-x}V_xO_3$. Crosses are raw data points, and curves are interpolations.

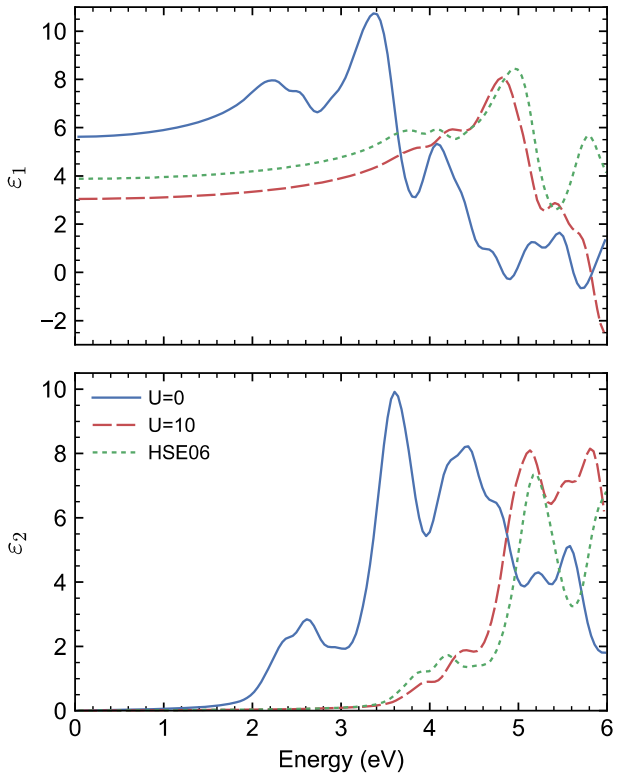

Fig. 3. Calculated complex dielectric function spectra ε_1 and ε_2 of $SrTiO_3$ with different parameter settings. The first two cases were calculated with PBE, and the last with HSE06.

of ε_2 at ~5.3 eV in Fig. 3, an O-p to Ti-e_g interband transition. However, such an energy value is beyond the blue end of the visible spectrum and does not affect our evaluation this material as a TCO. In addition, the shapes of respective Ti-d bands stay the same before and after the application of U value. On the other hand, HSE06 does not produce the correct results for $SrVO_3$, a metallic compound (see Supplemental Materials) to be mixed with $SrTiO_3$ in our study. Therefore we chose PBE/U = 10 eV for the study of electronic DOS and complex dielectric functions of random solid solutions. In short, the calculated complex dielectric function spectra and band structures demonstrate the effectiveness of this treatment, despite the unusually large chosen U value.

3.4. Electronic properties of random solid solutions

Fig. 5 shows the progression of local/projected DOS of $SrTi_{1-x}V_xO_3$ covering the full range of x modeled with SQS's. A few orbitals are plotted, including V-t_{2g}, V-e_g, Ti-t_{2g}, Ti-e_g and O-p. All other orbitals contribute little to bands between −8 eV and 5 eV. The first subplot corresponds to pure unit cells of $SrVO_3$. Due to the crystal field by the octahedrally coordinated O^{2-}, the five V-d orbitals of each V^{4+} split into three lower-lying V-t_{2g} states between −1 eV and 1.5 eV, and two higher-lying V-e_g states beyond 1 eV. V-t_{2g} states below E_F accommodate electrons and the states around E_F contribute to $SrVO_3$'s conductivity. The last subplot corresponds to $SrTiO_3$, the band structure of which is shown in Fig. 4(b) but with E_F adjusted to match with the other compositions. All Ti-d states lie above E_F, and the O^{2-} octahedral crystal field splitting also occurs to Ti^{4+}. In this case, Ti-t_{2g} states lie just a bit lower than Ti-e_g, almost within the same energy range between 1.3 and 4 eV, a result due to the GGA + U = 10 eV shift. Throughout the progression with decreasing x, V-d states keep diminishing in magnitude while Ti-d states keep increasing in magnitude, a natural outcome

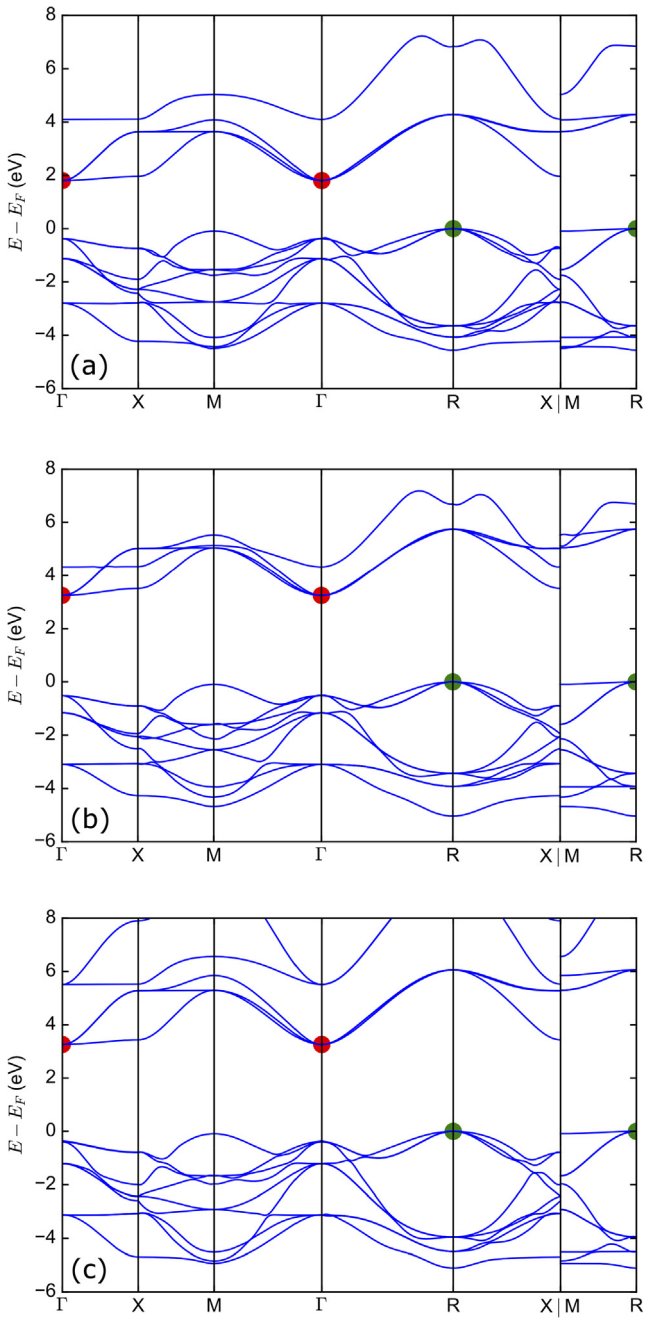

Fig. 4. Calculated band structures of $SrTiO_3$ with (a) PBE/U = 0 and (b) PBE/U = 10 eV, and (c) HSE06.

of cation substitution. O-p dominates the valence bands, and form bands together with the cation d states at energies depending on the composition of Ti^{4+} with respect to V^{4+}.

As x gets close to 0.67 (6/9), a valley at E_F develops, corresponding to the metal to insulator transition. Previous experimental studies found this composition to be the conduction limit. The conductivities of $SrVO_3$ (x = 0) and solid solution (x = 0.2) measure on the magnitude of 10^4 S/cm, and drop to 10^3 S/cm for x = 0.3, 10^2 S/cm for x = 0.5 [16–18]. This agrees well with the assumption brought by Tsuiki et al., that the V^{4+} octahedra in solid solutions go through Jahn-Teller distortion, and this splits the V-t_{2g} states even more, in addition to the O^{2-} crystal field splitting [16]. The valley at E_F thus corresponds to the gap between the lower and upper Hubbard bands. It is further substantiated by the calculation of V—O bond lengths and O—V—O bond angles in Fig. 6. Larger and larger

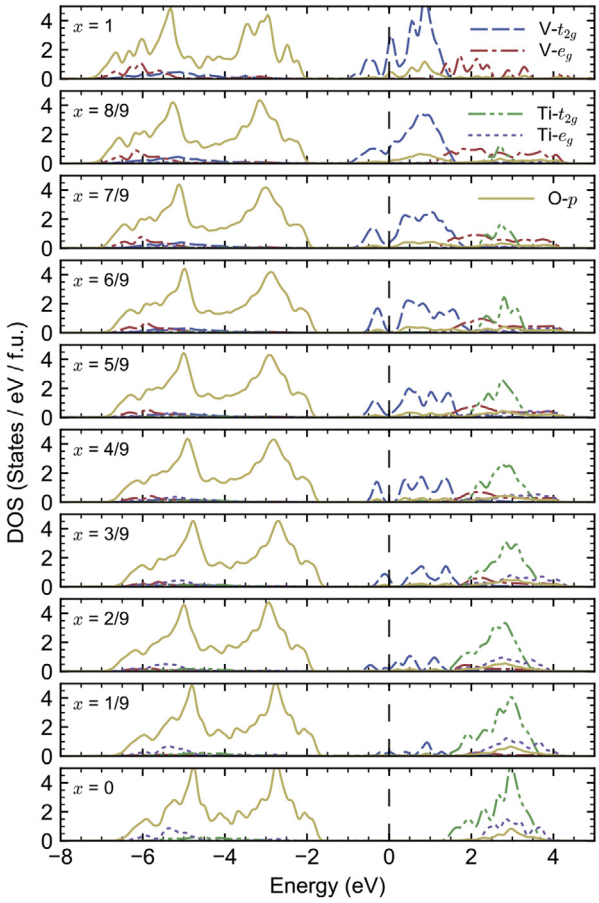

Fig. 5. Calculated projected density of states (DOS) of $SrTi_{1-x}V_xO_3$ with different compositions x. The Fermi energy has been set to 0, and the DOS of insulating $SrTiO_3$ has been aligned with the other compositions. Only V-t_{2g}, V-e_g, Ti-t_{2g}, Ti-e_g and O-p states are shown, because other states have minimal contributions.

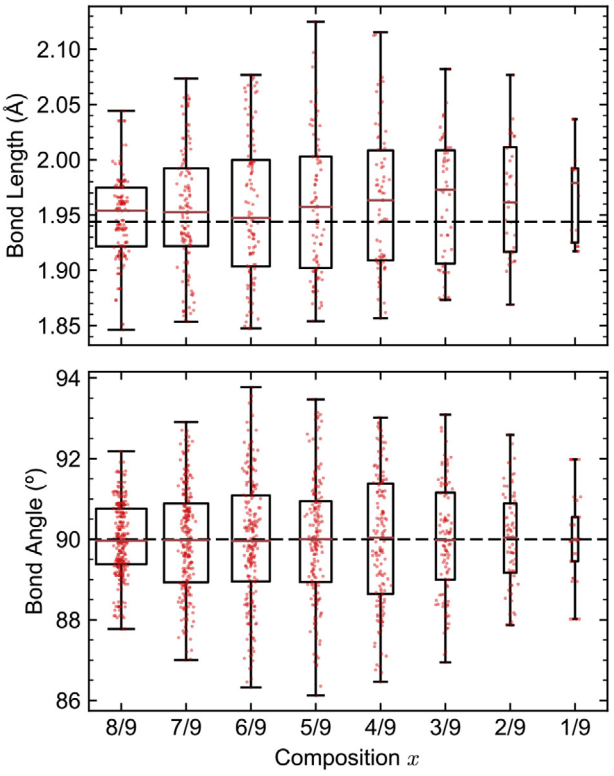

Fig. 6. Bond lengths of V—O, and bond angles of O—V—O in SQS's of $SrTi_{1-x}V_xO_3$ with different compositions x. Each box extends from the lower to upper quartile values, with a line at the median. The whiskers extend from the box to show the range of the data. Widths of the box are scaled with respect to numbers of data points. The slightly horizontally jittered red dots are actual values. The dashed lines correspond to values in the end member $SrVO_3$. (For interpretation of the references to colour in this figure legend, the reader is referred to the web version of this article.)

deviation from those in the end member $SrVO_3$ takes place as x decreases. The bonds get elongated and demonstrate more variation, resulting in larger volumes of the VO_6 octahedra, to accommodate for the total crystal volume increase caused by neighboring TiO_6. The same trend for volume is seen in Fig. S4 of the Supplemental Materials for the TiO_6 octahedra. This accommodation was also observed by Dawson et al. in their classical simulation of mixing $BaTiO_3$ with $CaTiO_3$ and $SrTiO_3$ [113], where the volumes of TiO_6 octahedra shrink as smaller cations, Ca^{2+}, Sr^{2+}, replace Ba^{2+}. The decrease in conductivity could also be related to increased ionicity with the decrease of x, as demonstrated by the Bader charge transfer analysis in Table 2. It indicates a slight and steady increase of transfer between Ti-O and V-O pairs with the replacement of V for Ti, turning the local environment of V and Ti more polarized, depleting available electrons from being conducting carriers. Note that in the traditional design approach for TCOs, dopant cations provide isolated states for wide-gap semiconductors, facilitating free carrier excitation. Similarly, this observation of electronic DOS progression opens doors to the possibility of doping other cations or creating vacancies to provide some states to fill in such a gap. Such an approach may enhance conductivity and extend the conducting compositions of $SrTi_{1-x}V_xO_3$ below x = 0.67.

Table 2
Bader charge transfer (e/atom) of SQS's of $SrTi_{1-x}V_xO_3$ with different compositions x.

x	Sr (e)	Ti (e)	V (e)	O (e)
1	−1.59		−2.11	1.24
8/9	−1.59	−2.52	−2.12	1.25
7/9	−1.60	−2.53	−2.12	1.27
6/9	−1.59	−2.53	−2.13	1.28
5/9	−1.59	−2.54	−2.13	1.30
4/9	−1.59	−2.54	−2.14	1.32
3/9	−1.59	−2.55	−2.14	1.33
2/9	−1.59	−2.55	−2.14	1.35
1/9	−1.59	−2.55	−2.15	1.37
0	−1.59	−2.55		1.38

3.5. Optical properties of random solid solutions

Fig. 7 shows the energy-dependent complex dielectric function spectra ε_1 and ε_2 of $SrTi_{1-x}V_xO_3$ with SQS's. Fig. 8 shows the absorption coefficients (α) obtained from spectra in ε ($\varepsilon = (n + ik)^{1/2}$; $\alpha = 4\pi k/\lambda$) up to 6.0 eV. The low-energy range below 2.00 eV can be largely attributed to intraband transitions and the high-energy range to interband transitions. As x becomes smaller, the shapes of ε_1 and ε_2 change continuously from resembling $SrVO_3$ to $SrTiO_3$. The critical point in ε_2 at 3.4 eV decreases in magnitude while other high energy features increase. When no low-energy phonon related transitions are present, the point at which $\varepsilon_1 = 0$ indicates the free carrier absorption edge. These values are predominantly between 0.5 eV and 1.5 eV. As soon as Ti^{4+} cations are introduced, this quantity blue-shifts from the pure $SrVO_3$'s 1.0 eV to ~1.5 eV, but still below 1.75 eV, the red end of the visible spectral range. This indicates intraband transitions are pushed to higher energies, but could also be an artifact of the calculation method, because even with a small replacement of V^{4+} for Ti^{4+} at x = 0.89 (8/9), the blue-shift is apparent and stays roughly the same with more replacements. On the other hand, the introduction of Ti^{4+} helps

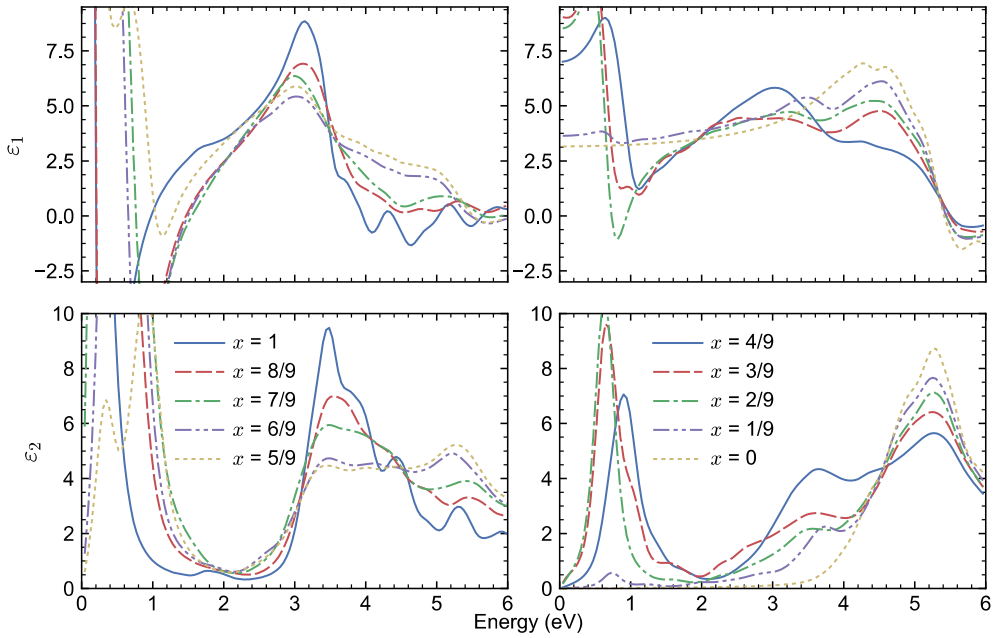

Fig. 7. Calculated complex dielectric function spectra ε_1 and ε_2 of SQS's of $SrTi_{1-x}V_xO_3$ with different compositions x.

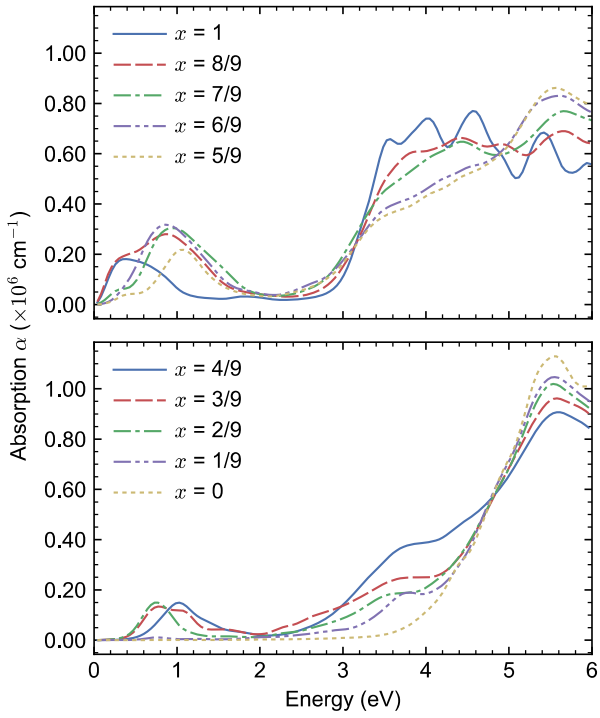

Fig. 8. Calculated absorption coefficient (α) spectra of SQS's of $SrTi_{1-x}V_xO_3$ with different compositions x.

suppress the absorption beyond the blue end of the visible range, 3.25 eV. Although the critical point in ε_2 at 3.4 eV does not blue-shift to open a wider transparency window, the transition strength decreases. Spectra in ε_2 at 3.4 eV when x = 0.67 (6/9) are approximately halved, effectively allowing more light beyond the blue end of the visible spectrum to pass through these compositions without being absorbed. There is also a slight absorption increase between 2.00 and 3.25 eV, likely due to the smoothing method involved. Therefore, solid solutions of 0.67 < x < 1 could be strong candidates for TCOs due to less high-energy photon absorption and only slightly reduced conductivity. As the system becomes Ti-rich (x < 0.67), the transparency window widens, but such solid solutions no longer retain the high conductivity required for their usual applications. As we discussed in Section 3.4, doping or vacancy creation could enhance conductivity and extend the conducting range of composition, allowing further absorption suppression beyond, or even below the blue end of the visible spectrum.

4. Conclusions

We studied the mixing of $SrVO_3$ and $SrTiO_3$ with CE, MC simulations and SQS. We confirmed with thermodynamics modeling the feasibility of obtaining solid solutions $SrTi_{1-x}V_xO_3$ across the full composition range ($0 \leq x \leq 1$). A simple miscibility gap closes at consolute temperature T_C = 500 K. Phase boundaries show slight asymmetry skewing toward the larger cation $SrTiO_3$-side. Electronic DOS and optical properties, including complex dielectric function spectra and band structures of random solid solutions were studied with SQS. Substitution of V with Ti reduces the electrical conductivity of $SrTi_{1-x}V_xO_3$, which goes through a composition-driven metal to insulator transition close to x = 0.67, but suppresses the optical absorption beyond 3.25 eV. It is likely that doping or vacancy creation would enhance the electrical conductivity and extend the conducting compositions, leaving room for property tuning to obtain optimal TCO materials.

Acknowledgement

The computing for this project was performed at the Tandy Supercomputing Center and Ohio Supercomputer Center (OSC) [114]. We thank the National Science Foundation grants CMMI 1234777 and 1629239 for funding this work.

Appendix A. Supplementary material

Supplementary data associated with this article can be found, in the online version, at https://doi.org/10.1016/j.commatsci.2017.12.020.

References

[1] L. Zhang et al., Correlated metals as transparent conductors, Nat. Mater. 15 (2016) 204–210.
[2] A.J. Freeman, K.R. Poeppelmeier, T.O. Mason, R.P.H. Chang, T.J. Marks, Chemical and thin-film strategies for new transparent conducting oxides, MRS Bull. 25 (2000) 45–51.
[3] K. Ellmer, Past achievements and future challenges in the development of optically transparent electrodes, Nat. Photon. 6 (2012) 809–817.
[4] H. Mizoguchi, T. Kamiya, S. Matsuishi, H. Hosono, A germanate transparent conductive oxide, Nat. Commun. 2 (2011) 470.
[5] T. Minami, Transparent conducting oxide semiconductors for transparent electrodes, Semicond. Sci. Technol. 20 (2005) S35–S44.
[6] W.F. Brinkman, T.M. Rice, Application of Gutzwiller's variational method to the metal-insulator transition, Phys. Rev. B 2 (1970) 4302–4304.
[7] J. Son et al., Low-dimensional mott material: transport in ultrathin epitaxial $LaNiO_3$ films, Appl. Phys. Lett. 96 (2010) 62114.
[8] I. Nagai et al., Highest conductivity oxide $SrMoO_3$ grown by a floating-zone method under ultralow oxygen partial pressure, Appl. Phys. Lett. 87 (2005) 24105.
[9] A. Radetinac, K.S. Takahashi, L. Alff, M. Kawasaki, Y. Tokura, Single-crystalline $CaMoO_3$ and $SrMoO_3$ films grown by pulsed laser deposition in a reductive atmosphere, Appl. Phys. Express 3 (2010) 73003.
[10] K. Fujita, T. Mochida, K. Nakamura, High-temperature thermoelectric properties of $Na_xCoO_{2-\delta}$ single crystals, Jpn. J. Appl. Phys. 40 (2001) 4644–4647.
[11] C.W. Hicks et al., Quantum oscillations and high carrier mobility in the delafossite $PdCoO_2$, Phys. Rev. Lett. 109 (2012) 116401.
[12] P.A. Lightsey, D.A. Lilienfeld, D.F. Holcomb, Transport properties of cubic Na_xWO_3 near the insulator-metal transition, Phys. Rev. B 14 (1976) 4730–4732.
[13] J.W. Tashman et al., Epitaxial growth of VO_2 by periodic annealing, Appl. Phys. Lett. 104 (2014) 63104.
[14] R.D. Shannon, Revised effective ionic radii and systematic studies of interatomic distances in halides and chalcogenides, Acta Crystallogr. Sect. A 32 (1976) 751–767.
[15] K. van Benthem, C. Elsässer, R.H. French, Bulk electronic structure of $SrTiO_3$: experiment and theory, J. Appl. Phys. 90 (2001) 6156.
[16] H. Tsuiki, K. Kitazawa, K. Fueki, The donor level of V4+ and the metal-nonmetal transition in $SrTi_{1-x}V_xO_3$, Jpn. J. Appl. Phys. 22 (1983) 590–596.
[17] K. Hong, S.-H. Kim, Y.-J. Heo, Y.-U. Kwon, Metal–insulator transitions of $SrTi_{1-x}V_xO_3$ solid solution system, Solid State Commun. 123 (2002) 305–310.
[18] M. Gu, S.A. Wolf, J. Lu, Metal-insulator transition in $SrTi_{1-x}V_xO_3$ thin films, Appl. Phys. Lett. 103 (2013) 223110.
[19] J.W.D. Connolly, A.R. Williams, Density-functional theory applied to phase-transformations in transition-metal alloys, Phys. Rev. B 27 (1983) 5169–5172.
[20] J.M. Sanchez, F. Ducastelle, D. Gratias, Generalized cluster description of multicomponent systems, Phys. A 128 (1984) 334–350.
[21] F. Ducastelle, Order and Phase Stability in Alloys, Elsevier Science, 1991.
[22] D.De. Fontaine, in: Solid State Physics - Advances in Research and Applications, vol 47, (1994) 33–176.
[23] A. Zunger, in: P.E. Turchi, A. Gonis (Eds.), NATO ASI on Statics and Dynamics of Alloy Phase Transformation, Plenum Press, 319, 361 (1994).
[24] D.B. Laks, L.G. Ferreira, S. Froyen, A. Zunger, Efficient cluster-expansion for substitutional systems, Phys. Rev. B 46 (1992) 12587–12605.
[25] W.Z. Chen, G.L. Xu, I. Martin-Bragado, Y.W. Cui, Non-empirical phase equilibria in the Cr-Mo system: a combination of first-principles calculations, cluster expansion and Monte Carlo simulations, Solid State Sci. 41 (2015) 19–24.
[26] J.Z. Liu, A. Zunger, Thermodynamic theory of epitaxial alloys: first-principles mixed-basis cluster expansion of (In, Ga)N alloy film, J. Phys.-Condens. Matter 21 (2009) 295402.
[27] G. Ghosh, A. van de Walle, M. Asta, First-principles calculations of the structural and thermodynamic properties of bcc, fcc and hcp solid solutions in the Al–TM (TM = Ti, Zr and Hf) systems: a comparison of cluster expansion and supercell methods, Acta Mater. 56 (2008) 3202–3221.
[28] J.Z. Liu, A. van de Walle, G. Ghosh, M. Asta, Structure, energetics, and mechanical stability of Fe-Cu bcc alloys from first-principles calculations, Phys. Rev. B 72 (2005) 144109.
[29] A. van de Walle, Z. Moser, W. Gasior, First-principles calculation of the Cu-Li phase diagram, Arch. Metall. Mater. 49 (2004) 535–544.
[30] M.C. Gao et al., Phase stability and elastic properties of Cr-V alloys, J. Phys.-Condens. Matter 25 (2013) 75402.
[31] S.V. Barabash, R.V. Chepulskii, V. Blum, A. Zunger, First-principles determination of low-temperature order and ground states of Fe-Ni, Fe-Pd, and Fe-Pt, Phys. Rev. B 80 (2009) 220201.
[32] C. Ravi, B.K. Panigrahi, M.C. Valsakumar, A. van de Walle, First-principles calculation of phase equilibrium of V-Nb, V-Ta, and Nb-Ta alloys, Phys. Rev. B 85 (2012) 54202.
[33] H.T. Xue et al., Phase equilibrium of a $CuInSe_2$-$CuInS_2$ pseudobinary system studied by combined first-principles calculations and cluster expansion Monte Carlo simulations, Mater. Sci. Semicond. Process. 25 (2014) 251–257.
[34] B.P. Burton, A. van de Walle, U. Kattner, First principles phase diagram calculations for the wurtzite-structure systems AlN–GaN, GaN–InN, and AlN–InN, J. Appl. Phys. 100 (2006) 113528.
[35] X.K. Li, H.T. Xue, F.L. Tang, W.J. Lu, First-principles calculation of sulfur-selenium segregation in $ZnSe_{1-x}S_x$: the role of lattice vibration, Mater. Sci. Semicond. Process. 39 (2015) 96–102.
[36] B.P. Burton, S. Demers, A. van de Walle, First principles phase diagram calculations for the wurtzite-structure quasibinary systems SiC-AlN SiC-GaN and SiC-InN, J. Appl. Phys. 110 (2011) 23507.
[37] B.P. Burton, A. van de Walle, First-principles phase diagram calculations for the system NaCl-KCl: the role of excess vibrational entropy, Chem. Geol. 225 (2006) 222–229.
[38] B.P. Burton, A. van de Walle, First principles phase diagram calculations for the octahedral-interstitial system αTiOX, $0 \leq X \leq 1/2$, Calphad 39 (2012) 97–103.
[39] B.P. Burton, A. van de Walle, First principles phase diagram calculations for the octahedral-interstitial system HfOX, $0 \leq X \leq 1/2$, Calphad 37 (2012) 151–157.
[40] B.P. Burton, A. van de Walle, H.T. Stokes, First principles phase diagram calculations for the octahedral-interstitial system ZrOX, $0 \leq X \leq 1/2$, J. Phys. Soc. Jpn. 81, (2012) 14004.
[41] Z.T.Y. Liu, B.P. Burton, S.V. Khare, D. Gall, First-principles phase diagram calculations for the rocksalt-structure quasibinary systems TiN–ZrN, TiN–HfN and ZrN–HfN, J. Phys. Condens. Matter 29 (2017) 35401.
[42] B.P. Burton, A. van de Walle, First-principles-based calculations of the $CaCO_3$-$MgCO_3$ and $CdCO_3$-$MgCO_3$ subsolidus phase diagrams, Phys. Chem. Miner. 30 (2003) 88–97.
[43] V.L. Vinograd, B. Winkler, A. Putnis, J.D. Gale, M.H.F. Sluiter, Static lattice energy calculations of mixing and ordering enthalpy in binary carbonate solid solutions, Chem. Geol. 225 (2006) 304–313.
[44] V.L. Vinograd, B.P. Burton, J.D. Gale, N.L. Allan, B. Winkler, Activity–composition relations in the system $CaCO_3$–$MgCO_3$ predicted from static structure energy calculations and Monte Carlo simulations, Geochim. Cosmochim. Acta 71 (2007) 974–983.
[45] V.L. Vinograd, M.H.F. Sluiter, B. Winkler, Subsolidus phase relations in the $CaCO_3$–$MgCO_3$ system predicted from the excess enthalpies of supercell structures with single and double defects, Phys. Rev. B 79 (2009) 104201.
[46] Z.T.Y. Liu, B.P. Burton, S.V. Khare, P. Sarin, First-principles phase diagram calculations for the carbonate quasibinary systems $CaCO_3$-$ZnCO_3$, $CdCO_3$-$ZnCO_3$, $CaCO_3$-$CdCO_3$ and $MgCO_3$-$ZnCO_3$, Chem. Geol. 443 (2016) 137–145.
[47] A. Zunger, S.H. Wei, L.G. Ferreira, J.E. Bernard, Special quasirandom structures, Phys. Rev. Lett. 65 (1990) 353–356.
[48] A. van de Walle et al., Efficient stochastic generation of special quasirandom structures, Calphad-Comp. Coup. Phase Diag. Thermochem. 42 (2013) 13–18.
[49] D.W. Shin, Z.K. Liu, Enthalpy of mixing for ternary fcc solid solutions from special quasirandorn structures, Calphad-Comp. Coup. Phase Diag. Thermochem. 32 (2008) 74–81.
[50] S.L. Shang et al., Structural, vibrational, and thermodynamic properties of ordered and disordered $Ni_{1-x}Pt_x$ alloys from first-principles calculations, Phys. Rev. B 83 (2011) 144204.
[51] D. Shin, A. van de Walle, Y. Wang, Z.-K. Liu, First-principles study of ternary fcc solution phases from special quasirandom structures, Phys. Rev. B 76 (2007) 144204.
[52] J. von Pezold, A. Dick, M. Friák, J. Neugebauer, Generation and performance of special quasirandom structures for studying the elastic properties of random alloys: application to Al-Ti, Phys. Rev. B 81 (2010) 94203.
[53] R. Sahara, S. Emura, S. Ii, S. Ueda, K. Tsuchiya, First-principles study of electronic structures and stability of body-centered cubic Ti–Mo alloys by special quasirandom structures, Sci. Technol. Adv. Mater. 15 (2014) 35014.
[54] D. Shin, R. Arróyave, Z.-K. Liu, A. Van de Walle, Thermodynamic properties of binary hcp solution phases from special quasirandom structures, Phys. Rev. B 74 (2006) 24204.
[55] F. Tasnádi, M. Odén, I.A. Abrikosov, Ab initio elastic tensor of cubic Ti 0.5 Al 0.5 N alloys: dependence of elastic constants on size and shape of the supercell model and their convergence, Phys. Rev. B 85 (2012) 144112.
[56] Y. Hinuma, F. Oba, Y. Nose, I. Tanaka, First-principles study of valence band offsets at ZnSnP2/CdS, ZnSnP2/ZnS, and related chalcopyrite/zincblende heterointerfaces, J. Appl. Phys. 114 (2013) 6.
[57] D. Usanmaz et al., First principles thermodynamical modeling of the binodal and spinodal curves in lead chalcogenides, Phys. Chem. Chem. Phys. 18 (2015) 5005–5011.
[58] B. Alling, Theory of the ferromagnetism in $Ti_{1-x}Cr_xN$ solid solutions, Phys. Rev. B 82 (2010) 54408.
[59] B. Alling, T. Marten, I.A. Abrikosov, A. Karimi, Comparison of thermodynamic properties of cubic $Cr_{1-x}Al_xN$ and $Ti_{1-x}Al_xN$ from first-principles calculations, J. Appl. Phys. 102 (2007) 44314.
[60] B. Alling et al., Mixing and decomposition thermodynamics of c-$Ti_{1-x}Al_xN$ from first-principles calculations, Phys. Rev. B 75 (2007) 45123.
[61] B. Alling, A. Karimi, L. Hultman, I.A. Abrikosov, First-principles study of the effect of nitrogen vacancies on the decomposition pattern in cubic $Ti_{1-x}Al_xN_{1-y}$, Appl. Phys. Lett. 92 (2008) 71903.
[62] B. Alling, L. Hultberg, L. Hultman, I.A. Abrikosov, Strong electron correlations stabilize paramagnetic cubic $Cr_{1-x}Al_xN$ solid solutions, Appl. Phys. Lett. 102 (2013) 31910.
[63] D. Holec et al., Macroscopic elastic properties of textured ZrN-AlN polycrystalline aggregates: from ab initio calculations to grain-scale interactions, Phys. Rev. B 90 (2014) 184106.
[64] D. Holec, F. Rovere, P.H. Mayrhofer, P.B. Barna, Pressure-dependent stability of cubic and wurtzite phases within the TiN-AlN and CrN-AlN systems, Scr. Mater. 62 (2010) 349–352.

[65] D. Holec, R. Franz, P.H. Mayrhofer, C. Mitterer, Structure and stability of phases within the NbN–AlN system, J. Phys. D Appl. Phys. 43 (2010) 145403.
[66] L. Zhou, D. Holec, P.H. Mayrhofer, First-principles study of elastic properties of cubic $Cr_{1-x}Al_xN$ alloys, J. Appl. Phys. 113 (2013) 43511.
[67] L. Zhou, D. Holec, P.H. Mayrhofer, Ab initio study of the alloying effect of transition metals on structure, stability and ductility of CrN, J. Phys. D Appl. Phys. 46 (2013) 365301.
[68] L. Zhou et al., Structural stability and thermodynamics of CrN magnetic phases from ab initio calculations and experiment, Phys. Rev. B 90 (2014) 184102.
[69] I. Efthimiopoulos et al., Structural transition in the magnetoelectric $ZnCr_2Se_4$ spinel under pressure, Phys. Rev. B 93 (2016) 174103.
[70] I. Efthimiopoulos et al., Pressure-induced phase transitions in the $CdCr_2Se_4$ spinel, Phys. Rev. B 94 (2016) 174106.
[71] I. Efthimiopoulos et al., Pressure-induced transition in the multiferroic $CoCr_2O_4$ spinel, Phys. Rev. B 92 (2015) 64108.
[72] B.K. Voas et al., Special quasirandom structures to study the $(K0.5Na0.5)NbO_3$ random alloy, Phys. Rev. B 90 (2014) 24105.
[73] Z. Jiang et al., Special quasirandom structures for perovskite solid solutions, J. Phys. Condens. Matter 28 (2016) 475901.
[74] G. Kresse, J. Furthmuller, Efficiency of ab-initio total energy calculations for metals and semiconductors using a plane-wave basis set, Comput. Mater. Sci. 6 (1996) 15–50.
[75] G. Kresse, J. Furthmuller, Efficient iterative schemes for ab initio total-energy calculations using a plane-wave basis set, Phys. Rev. B 54 (1996) 11169–11186.
[76] G. Kresse, J. Hafner, Ab initio molecular-dynamics simulation of the liquid-metal–amorphous-semiconductor transition in germanium, Phys. Rev. B 49 (1994) 14251–14269.
[77] G. Kresse, J. Hafner, Ab initio molecular dynamics for liquid metals, Phys. Rev. B 47 (1993) 558–561.
[78] P.E. Blöchl, Projector augmented-wave method, Phys. Rev. B 50 (1994) 17953–17979.
[79] G. Kresse, D. Joubert, From ultrasoft pseudopotentials to the projector augmented-wave method, Phys. Rev. B 59 (1999) 1758–1775.
[80] J.P. Perdew et al., Atoms, molecules, solids, and surfaces - applications of the generalized gradient approximation for exchange and correlation (vol 46, Pg 6671, 1992), Phys. Rev. B 48 (1993) 4978.
[81] J.P. Perdew et al., Atoms, molecules, solids, and surfaces: applications of the generalized gradient approximation for exchange and correlation, Phys. Rev. B 46 (1992) 6671–6687.
[82] L. Wang, T. Maxisch, G. Ceder, Oxidation energies of transition metal oxides within the GGA + U framework, Phys. Rev. B 73 (2006) 195107.
[83] A. Jain et al., Formation enthalpies by mixing GGA and GGA + U calculations, Phys. Rev. B - Condens. Matter Mater. Phys. 84 (2011) 45115.
[84] S.P. Ong et al., Python materials genomics (pymatgen): a robust, open-source python library for materials analysis, Comput. Mater. Sci. 68 (2013) 314–319.
[85] F. Birch, Finite elastic strain of cubic crystals, Phys. Rev. 71 (1947) 809–824.
[86] Z.T.Y. Liu, X. Zhou, S.V. Khare, D. Gall, Structural, mechanical and electronic properties of 3d transition metal nitrides in cubic zincblende, rocksalt and cesium chloride structures: a first-principles investigation, J. Phys.-Condens. Matter 26 (2014) 25404.
[87] Z.T.Y. Liu, X. Zhou, D. Gall, S.V. Khare, First-principles investigation of the structural, mechanical and electronic properties of the NbO-structured 3d, 4d and 5d transition metal nitrides, Comput. Mater. Sci. 84 (2014) 365–373.
[88] I. Efthimiopoulos et al., High-pressure studies of Bi_2S_3, J. Phys. Chem. A 118 (2014) 1713–1720.
[89] X. Zhou, J.L. Roehl, C. Lind, S.V. Khare, Study of B1 (NaCl-type) to B2 (CsCl-type) pressure-induced structural phase transition in BaS, BaSe and BaTe using ab initio computations, J. Phys. Condens. Matter 25 (2013) 75401.
[90] A. van de Walle, M. Asta, G. Ceder, The alloy theoretic automated toolkit: a user guide, Calphad-Comp. Coup. Phase Diag. Thermochem. 26 (2002) 539–553.
[91] A. van de Walle, Multicomponent multisublattice alloys, nonconfigurational entropy and other additions to the alloy theoretic automated toolkit, Calphad-Comp. Coup. Phase Diag. Thermochem. 33 (2009) 266–278.
[92] A. van de Walle, M. Asta, Self-driven lattice-model Monte Carlo simulations of alloy thermodynamic properties and phase diagrams, Model. Simul. Mater. Sci. Eng. 10 (2002) 521–538.
[93] A. van de Walle, G. Ceder, Automating first-principles phase diagram calculations, J. Phase Equilibria 23 (2002) 348–359.
[94] Y.C. Lan, X.L. Chen, M. He, Structure, magnetic susceptibility and resistivity properties of $SrVO_3$, J. Alloys Compd. 354 (2003) 95–98.
[95] T. Mitsui, S. Nomura, Numerical Data and Functional Relations in Science and Technology-Crystal and Solid State Physics, Landoldt-Börnstein, New Series, Group III 16, (Springer-Verlag, 1982).
[96] Z.T.Y. Liu, D. Gall, S.V. Khare, Electronic and bonding analysis of hardness in pyrite-type transition-metal pernitrides, Phys. Rev. B 90 (2014) 134102.
[97] Y. Wang et al., Thermal equation of state of silicon carbide, Appl. Phys. Lett. 108 (2016) 61906.
[98] X. Zhou, D. Gall, S.V. Khare, Mechanical properties and electronic structure of anti-ReO_3 structured cubic nitrides, M3N, of d block transition metals M: an ab initio study, J. Alloys Compd. 595 (2014) 80–86.
[99] L. Gharaee, P. Erhart, P. Hyldgaard, Finite-temperature properties of nonmagnetic transition metals: comparison of the performance of constraint-based semilocal and nonlocal functionals, Phys. Rev. B 95 (2017) 85147.
[100] C. Stampfl, W. Mannstadt, R. Asahi, A.J. Freeman, Electronic structure and physical properties of early transition metal mononitrides: density-functional theory LDA, GGA, and screened-exchange LDA FLAPW calculations, Phys. Rev. B 63 (2001) 155106.
[101] Y.-M. Juan, E. Kaxiras, Application of gradient corrections to density-functional theory for atoms and solids, Phys. Rev. B 48 (1993) 14944–14952.
[102] E. Ateser, H. Ozisik, K. Colakoglu, E. Deligoz, The structural and mechanical properties of CdN compound: a first principles study, Comput. Mater. Sci. 50 (2011) 3208–3212.
[103] C.Z. Fan et al., Low compressible noble metal carbides with rocksalt structure: Ab initio total energy calculations of the elastic stability, Appl. Phys. Lett. 89 (2006) 71913.
[104] A.L. Ivanovskii, Mechanical and electronic properties of diborides of transition 3d–5d metals from first principles: toward search of novel ultra-incompressible and superhard materials, Prog. Mater. Sci. 57 (2012) 184–228.
[105] Z. Wu, J. Meng, Ab initio study on the physical properties of CoN_3 and RhN_3 with skutterudite structure, Comput. Mater. Sci. 43 (2008) 495–500.
[106] Y. Yang, H. Lu, C. Yu, J.M. Chen, First-principles calculations of mechanical properties of TiC and TiN, J. Alloys Compd. 485 (2009) 542–547.
[107] Z. Wu, R.E. Cohen, D.J. Singh, Comparing the weighted density approximation with the LDA and GGA for ground-state properties of ferroelectric perovskites, Phys. Rev. B 70 (2004) 104112.
[108] D.J. Singh, Local density and generalized gradient approximation studies of $KNbO_3$ and $BaTiO_3$, Ferroelectrics 164 (1995) 143–152.
[109] A.R. Oganov, J.P. Brodholt, G.D. Price, Ab initio elasticity and thermal equation of state of $MgSiO_3$ perovskite, Earth Planet. Sci. Lett. 184 (2001) 555–560.
[110] P. Haas, F. Tran, P. Blaha, Calculation of the lattice constant of solids with semilocal functionals, Phys. Rev. B 79 (2009) 85104.
[111] S.F. Yuk et al., Towards an accurate description of perovskite ferroelectrics: exchange and correlation effects, Sci. Rep. 7 (2017) 43482.
[112] I.R. Shein, V.L. Kozhevnikov, A.L. Ivanovskii, First-principles calculations of the elastic and electronic properties of the cubic perovskites $SrMO_3$ (M = Ti, V, Zr and Nb) in comparison with $SrSnO_3$, Solid State Sci. 10 (2008) 217–225.
[113] J.A. Dawson, D.C. Sinclair, J.H. Harding, C.L. Freeman, A-site strain and displacement in $Ba_{1-x}Ca_xTiO_3$ and $Ba_{1-x}Sr_xTiO_3$ and the consequences for the curie temperature, Chem. Mater. 26 (2014) 6104–6112.
[114] Ohio Supercomputer Center. (1987). Available at: <http://osc.edu/ark:/19495/f5s1ph73>.